Operator Theory:
Advances and Applications, Vol. 51

Application of Transport Theory to Infra-Red Medical Imaging

Raphael Aronson[1], Randall L. Barbour[2], Jack Lubowsky[2], and Harry Graber[2]
[*Conference presentation by R. Aronson*]

[1] Physics Department
Polytechnic University
Brooklyn, N.Y. 11201

[2] SUNY Health Sciences Center at Brooklyn
Brooklyn, N.Y. 11203

Abstract

We discuss the principles of a potential imaging scheme which makes use of reflected radiation in the near infrared region and is intended for a broad spectrum of clinical applications. The object is to detect and image regions of anomalous absorption, which give information about physiological function. We describe Monte Carlo procedures used to simulate the process and give computed results for weight functions. Computed images of simulated absorbers are also presented. We discuss possible applications.

I. Introduction and Background

The past several years have seen the development of a variety of techniques for medical imaging that have become standard clinical procedures. Among these are computer-aided tomography (CAT), magnetic resonance imaging (MRI), ultrasound and positron emission tomography (PET). These various techniques involve very different physical principles and give very different sorts of information. Although they give highly useful knowledge concerning the structure of body tissues, with the possible exception of PET they give no information concerning functional properties. In this paper we consider a model of photon transport in tissue together with an analysis scheme which may be used as a basis for imaging a critical functional property common to all body tissues, namely, the relation between organ function and oxidative metabolism. [1]

The clinical problem arises from the fact that body tissues are highly dependent on aerobic metabolism function and can die if they are deprived of sufficient oxygen for more than a few minutes. The two key substances involved are hemoglobin and the enzyme cytochrome oxidase. Hemoglobin carries oxygen from the lungs through the vascular network, becoming

deoxygenated in the capillaries and ultimately delivering its oxygen to cytochrome oxidase. In the mitochrondia cytochrome oxidase reduces molecular oxygen to water, liberating chemical energy which can be captured by oxidative phosphorylation to yield ATP.

When supply-demand equilibrium is established in healthy tissues, typically greater than 90 per cent of the cytochrome oxidase is in the oxidized state. If the amount of oxygen delivered by the hemoglobin is not sufficient to meet the metabolic demand, the fraction of oxidized cytochrome oxidase can become dangerously low. This happens if the working muscles use oxygen inefficiently or if the supply of oxygen is insufficient. This situation will result in a low ratio of oxygenated to deoxygenated hemoglobin, among other things. It follows that the oxygenation state of these two substances is an important indicator of adequacy of function.

The physical basis for the use of near infra-red (NIR) radiation ($\sim$ 750-900 nm) is twofold. First, body tissue is relatively transparent to these wavelengths, as might be suggested by the fact that one can shine a flashlight through the hand and get light, diffuse as it is, out the other side. A typical transport mean free path is of the order of several millimeters. The second point is that there is a substantial difference in the cross sections, especially that for absorption, of both hemoglobin and cytochrome oxidase in this range. Figure 1 shows extinction coefficients for both oxygenated and deoxygenated forms of hemoglobin. The difference is striking. Figure 2 shows the change in the logarithm of the fraction of infrared light transmitted through a rat brain when the rat breathed nitrogen rather than oxygen. It is presumably due to the change in the oxidation state of cytochrome oxydase. The ordinate is not in absolute units. Both Fig. 1 and Fig. 2 are based on data of Wray et al. [2]

The ultimate object of our work is to locate and image regions of oxygen-deficient hemoglobin and cytochrome oxidase in tissue. This involves determining the distribution of reflected NIR radiation and using this information to determine regions of absorption inhomogeneities. We wish both to image such regions and to determine the degree of deoxidation within them. One major advantage of using infrared radiation is that one can envision a bedside instrument which could, for instance, be used in the operating room, in contrast with the big expensive fixed installations characteristic of CAT, PET and MRI measurements. Our goal is to develop a noninvasive, nondestructive, convenient measuring technique.

The idea is to irradiate the patient with a laser beam and scan the reflected radiation in both position and direction, move the source a number of times and repeat, analyzing the data by in effect solving an inverse problem. To this end we are carrying out both an experimental and a calculational program. In both the early experiments and in the analysis we are starting by considering a slab or half-space irradiated with a searchlight source normal to the surface. The medium is taken to be homogeneous except for one or more regions of different absorption cross section.

II. The Calculations

The calculations use a Monte Carlo technique to simulate the experiments, both as a basis for verifying our understanding of the experiments and as something to be normalized to experiment in some way. The medium is taken to consist of pointlike molecules with a

mean free path of the order of a few millimeters. While this is certainly wrong from the point of view of first principles, since the interatomic spacing is in fact small compared to the wavelength, we have chosen (along with almost all workers in the field) to avoid the complications of doing wave optics in a random medium at this time. The validity of this approximation must be checked a posteriori. We expect it to give a distorted image, which we assume can be corrected empirically.

The geometry is shown in Figure 3. A searchlight (point collimated) source at the origin points downward (toward increasing z), and a point collimated detector at (R,0,0) in cylindrical coordinates measures the outgoing flux in direction (θ, ϕ). In these calculations we assume isotropic scattering. The unit of length is the mean free path.

III. The Weight Function

In the linear approximation, the decrease in the measured flux at the detector is given by the expression

$$\Delta\phi_d = \int \Sigma_{a'}(\mathbf{r})\phi(\mathbf{r})P(\mathbf{r})d\mathbf{r} = \int \Sigma_{a'}(\mathbf{r})W(\mathbf{r})d\mathbf{r}.$$

The integral is over the volume of the medium. Here $\Delta\phi_d$ is the decrease of the flux at the detector due to absorption in excess of the uniform background (zero-order) absorption; $\Sigma_{a'}(\mathbf{r})$ is the excess local absorption cross section at $\mathbf{r}$; ϕ is the interior flux at $\mathbf{r}$; and P is the flux at the detector due to one photon born at $\mathbf{r}$ per unit time. In the linear approximation, ϕ and P are taken to be those for the background medium with an assumed small but uniform absorption cross section. In our calculations we have computed ϕ and P assuming a homogeneous background. Note that strictly P should depend on the direction of the source at $\mathbf{r}$. It helps enormously in the statistics if we can assume that this direction is uncorrelated in the equation with the direction of the photon arriving at $\mathbf{r}$, as it is for isotropic scattering, and as we assume. By reciprocity, P is the flux at $\mathbf{r}$ due to a unit source at (R,0,0) in direction $(\pi - \theta, \pi + \phi)$. Thus ϕ and P are found by identical Monte Carlo calculations for the interior flux due to a point monodirectional source. Their product W($\mathbf{r}$) is a weight function giving the importance of the point $\mathbf{r}$ to a decrease of the flux measured by the detector.

This is just the usual prescription that in perturbation theory the importance of a point is the product of the flux and adjoint at the point. [3]

Figures 4–9 show traces in various planes of contour surfaces of accumulated weight. In each case the detector is at (50,50,0) and the source at (55,50,0). In all the figures shown, $\theta = 30°$, $\phi = 0°$. This means that the source and detector directions are in the same vertical plane and the detector is tilted toward the source by 30°. Of course there is ambiguity in the presentation we have chosen. When one wants to fill in a contour by adding a region with a little more weight, where should this region be taken from? The criterion we use is that the regions are chosen to be as compact as possible.

Figures 4–6 show contour traces for the average weight function in a one-unit-thick vertical slab parallel to the source-detector plane. In Fig. 4 the slab extends from y=49.5 to y=50.5, so that it includes the source-detector plane; in Fig. 5 it extends from y=51.5 to y=52.5; in Fig. 6, from y=53.5 to y=54.5. In each region the accumulated weight is the indicated

percentage of the total amount. For a plane close to source and detector, the high weights are along the source and detector lines, one region near each. Lower-weight regions tend to be more uniform, as one might expect.

Figures 7–9 show the same kind of data for a set of one-unit-thick horizontal slabs, centered respectively 0.5, 2.5 and 6.5 mean free paths below the surface. For both the vertical and horizontal cuts, we see that the contours tend to have less structure, to look more and more like concentric spheres (or distorted spheres) as the slice recedes from source and detector.

IV. Simulation of Detection by Collimated Detectors

The experiments were simulated with a series of Monte Carlo calculations for reflected radiation in which the results were broken up into bins characterized by both distance from the source and direction. For these we used a last-collision statistical estimation procedure. The photons are not permitted to be killed by absorption and they are forced to collide within the medium. The loss processes are taken care of by reducing the weight. There is a Russian Roulette procedure that is invoked when the weight gets too low (we used 0.2 in the calculations to date). This is the only way in which particle histories can terminate. The difficulty with this calculation is that to get reasonable statistics in reasonable times, one must use bins with very large acceptance angles, losing much potentially available information.

To remedy this, we formulated the problem to force photons into infinitely narrow, collimated detectors in order to get exact angular and position-dependent reflected fluxes for a finite number of detectors. The geometry is shown in Fig. 10. Forcing the photons into a detector requires that the last collision occur along the ray leading to the detector. That is, the last collision point is determined by a single parameter. A two-last-flight estimator is required. At each collision point we then ask for the probability of reaching the detector with exactly one more collision, along the detector ray. Again, histories end only by losing the Russian Roulette game. We have done these calculations computing the estimator both by numerical integration and by random sampling on one variable that gives the last collision point. The numerical integration is too slow to be practicable. We use the same trajectories for all the detectors, computing different estimators for each.

The estimator for isotropic scattering is, for a half space,

$$W_n = W_{n-2}\left(\frac{\Sigma_s}{4\pi\Sigma_t}\right)^2 \int_o^\infty e^{-\Sigma_t(s+s')}\frac{ds}{s'^2}.$$

Here Σ_s is the macroscopic scattering cross section; Σ_t is the macroscopic total cross section; μ is the cosine of the detector direction angle with the normal; s' is the distance from the next-to-last collision point to the last collision point; and s is the distance from the last collision point to the surface at the detector. There is a Σ_s/Σ_t factor to account for the survival probability and one $1/4\pi$ factor for the isotropic scattering probability into unit solid angle for each of the last two collisions. The exponentials take into account absorption along the last two legs. There is also an inverse square factor along the next-to-last leg that converts photons per steradian per second at the last collision point to flux. This factor is not necessary at the detector, since we want photons per steradian per second. If the medium is

a slab rather than a half-space, the upper limit on the integral must be adjusted accordingly, as it must on the integral below.

Originally we also sampled randomly on s from the exponential distribution. In this case the estimator is

$$W_n = W_{n-2}(\frac{\Sigma_s}{4\pi\Sigma_t})^2 e^{-\Sigma_t s'}/s'^2.$$

This is an obvious sampling scheme, but it leads to infinite variance (and therefore unreliable results) because of the inverse square term. The difficulty comes from the very large weight when the last two collisions are very close together. An alternative expression for the estimator is

$$W_n = 2W_{n-2}(\frac{\Sigma_s}{4\pi\Sigma_t})^2 \frac{e^{-\Sigma_t \ell}}{p} \int_{\alpha(0)}^{\pi} e^{-\Sigma_t p \tan\alpha} d\alpha.$$

Here (see Fig. 10) p is the perpendicular distance from the next-to-last collision point to the exiting ray to the detector; ℓ is the directed distance from the foot of the perpendicular to the exit point at the detector, taken positive if $z > 0$ at the foot and negative if $z < 0$ at the foot; $cos2\alpha = \hat{\Omega} \cdot \hat{\Omega}'$.

Sampling on α gives a finite-variance estimator. The present scheme samples uniformly on α, though there is much reason to believe that this is not optimal. Results from this version of Monte Carlo are just beginning to come in, and we do not present any here. The calculation is quite slow, but some obvious improvements in the sampling scheme present themselves.

It is thought by many that because of the ill-conditioned nature of the inverse problem (or in more physical terms, because the reflected distribution is so insensitive to changes in absorption deep in the medium), that reasonable images can't be obtained. Figs. 11 and 12 show that localized absorbers can indeed be imaged. Figure 11 shows an image of the absorbers in the horizontal slab z=4–5, and Fig. 12 gives the image in the slab z=11–12. These results used the first Monte Carlo version described above, with finite (actually rather large) angular bins. The absorbers are black cubes, 2 mfp on a side, arranged symmetrically at the corners of a 6x6x6 cube, at z=4–6 and 8–10 centered about (x, y)=(50,50). It can be seen that the absorbers are detected and located more or less correctly, with a lot of fuzziness and distortion.

It must be remarked that the processing is computation-intensive. The results shown used 41 source positions, three detector angles (all in the source-detector plane) and 317 detector locations, and full advantage was taken of the symmetry. Since this was a first try at imaging a complex absorber, we chose a symmetric configuration in order to ease the data-handling problem. Clearly, this is an area for further work.

The imaging algorithm is the following: Let ϕ_j = angular flux at detector j in presence of absorber; ϕ_j^0 = angular flux at detector j in absence of absorber; W_{ij}^k = weight function for voxel i, detector j and source k. The relative darkening due to an absorption in voxel i is then taken to be

$$1 - (\sum_{j,k} W_{ij}^k \phi_j/\phi_j^0)/(\sum_{j,k} W_{ij}^k).$$

Here $W_{ij}^k = \int W_j^k(\mathbf{r})d\mathbf{r}$, integrated over the volume of voxel i, where we have explicitly gone to a discrete description. This algorithm is not derived on any systematic grounds, but

it does have the virtue of simplicity and demonstrates clearly that imaging is feasible, at least from calculated data. More sources, more detectors, calculations for truly collimated detectors and a better imaging algorithm should improve the results considerably.

V. Questions and Prospects

Among the major questions to be answered are:

(1) How weak an absorber, and how small an absorber, can be detected?
(2) What is the resolution, as a function of absorber strength, size and separation?
(3) How are experimental results best compared with calculated base cases? To the extent that the properties of the real and assumed medium differ, images will be shifted and distorted. What does this do to the resolution and to what extent can we correct for it?

The unique utility of a backscattering technique is that it doesn't require a large detector on the far side, so it can be used in acute clinical care. It is a remote sensing technique involving a noninvasive, nondestructive method of imaging that will permit several things. For instance:

(1) During surgery, the anesthesiologist can determine unambiguously the oxygenation state of the brain.
(2) It can be used for a definitive diagnosis of myocardial infarction or stroke.
(3) It is likely to be exceedingly useful for diagnosis and for monitoring response to therapy.
(4) It can allow real-time assessment of the oxidation state of a fetus in utero just prior to delivery.
(5) It could replace mammography for the diagnosis of breast cancer, since the oxidation state of solid tumors is very different from that of healthy tissue.

Thus it appears that one can obtain images from backscattering measurements which can be applied to derive functional information about body tissues. To use the information in this way one will have to do spectroscopy–that is, to employ several different wavelengths for illumination and comparing the images. The image can be improved not only is the ways mentioned above but also by using iterative and other standard image enhancement techniques. Further, even a very rough image, perhaps with a resolution of a few centimeters, can be very useful.

References

[1] M. Tamura, O. Hazeki, S. Nioka and B. Chance, Ann. Rev. Physiol. **51**, 813 (1989).

[2] S. Wray, M. Cope, D.T. Delpy, J.S. Wyatt and E.O.R. Reynolds, Biochim. Biophys. Acta **933**, 184 (1988).

[3] J. R. Lamarsh, *Nuclear Reactor Theory*, Addison-Wesley, Reading, Mass., 1966.

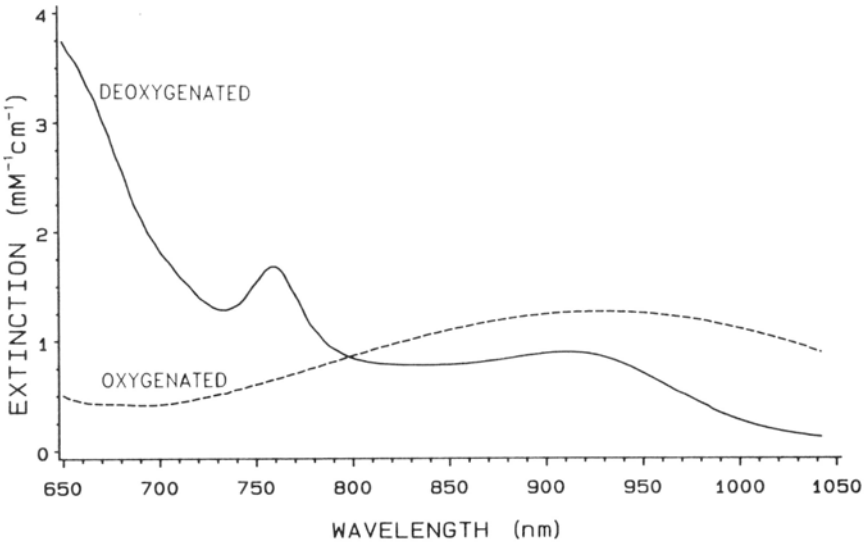

Fig. 1. Extinction Coefficient for Hemoglobin

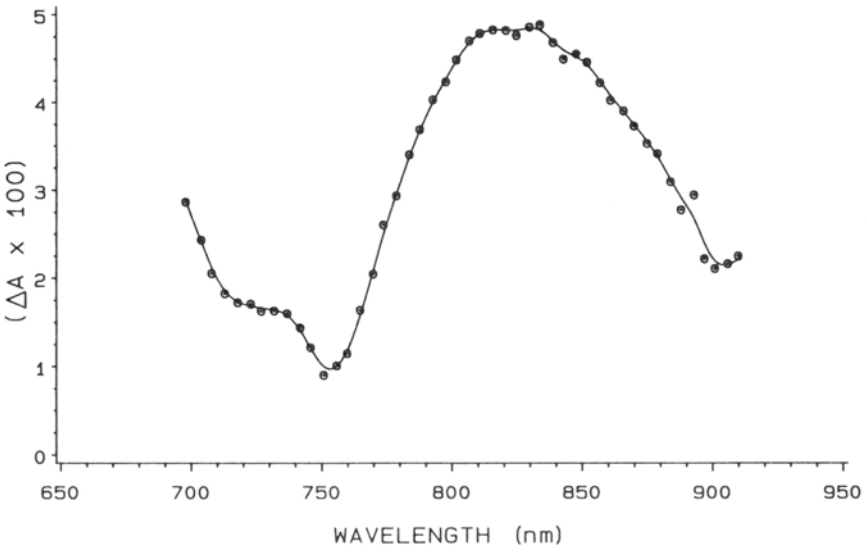

Fig. 2. Relative Difference in Extinction Coefficients in Oxidized and Deoxidized Cytochrome Oxidase

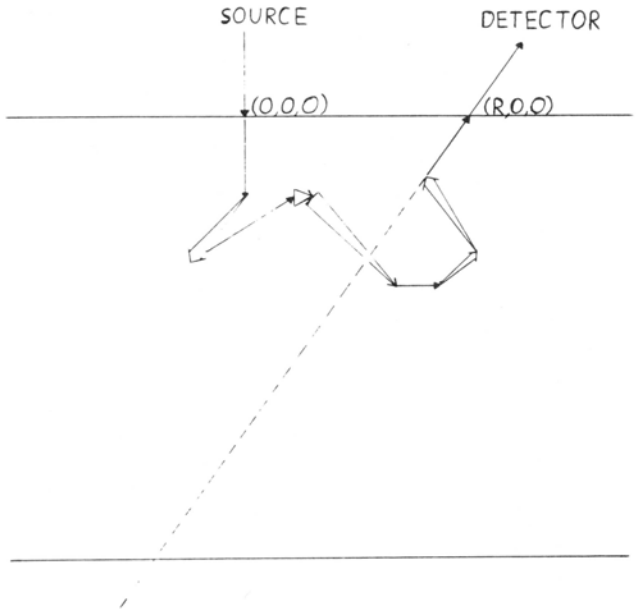

Fig. 3. Source–Detector Geometry

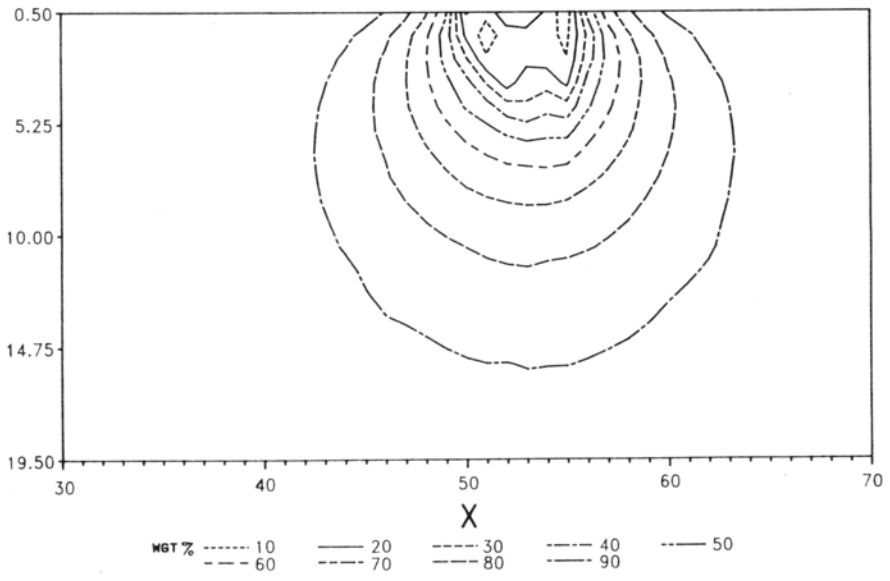

Fig. 4. Relative Weight Function, Detector Angle 30°, for Slab y=49.5–50.5

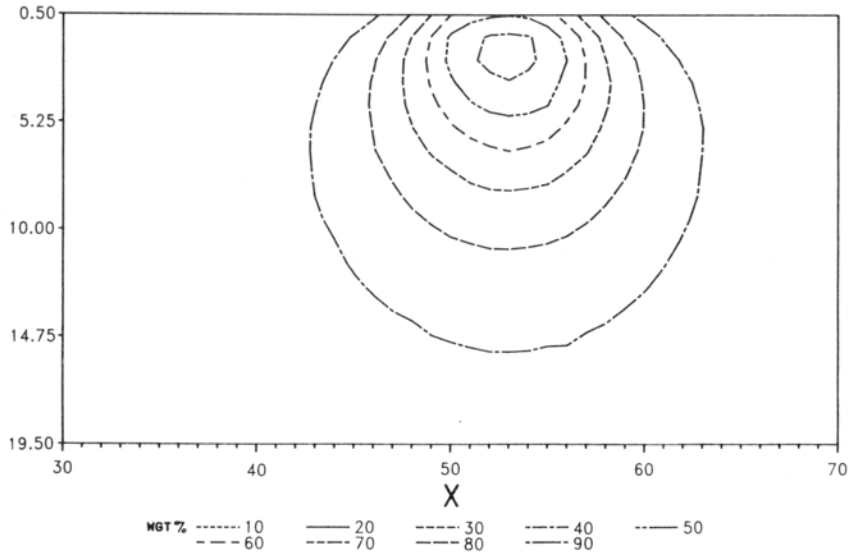

Fig. 5. Relative Weight Function, Detector Angle 30°, for Slab y=51.5–52.5

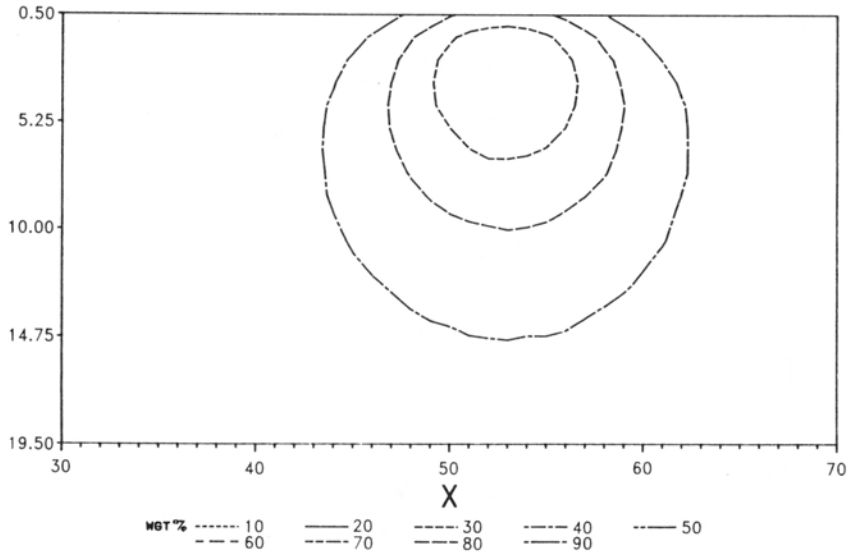

Fig. 6. Relative Weight Function, Detector Angle 30°, for Slab y=53.5–54.5

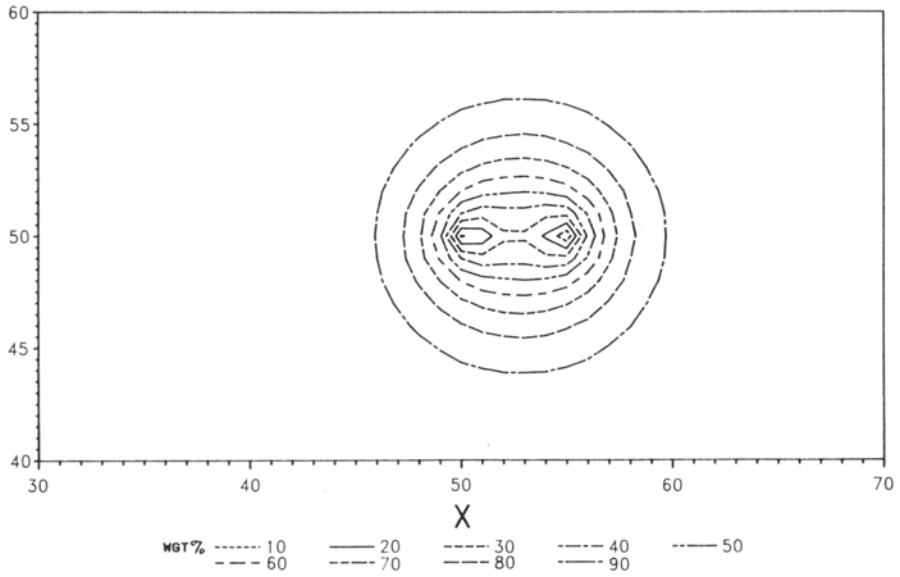

Fig. 7. Relative Weight Function, Detector Angle 30°, for Slab z=0–1

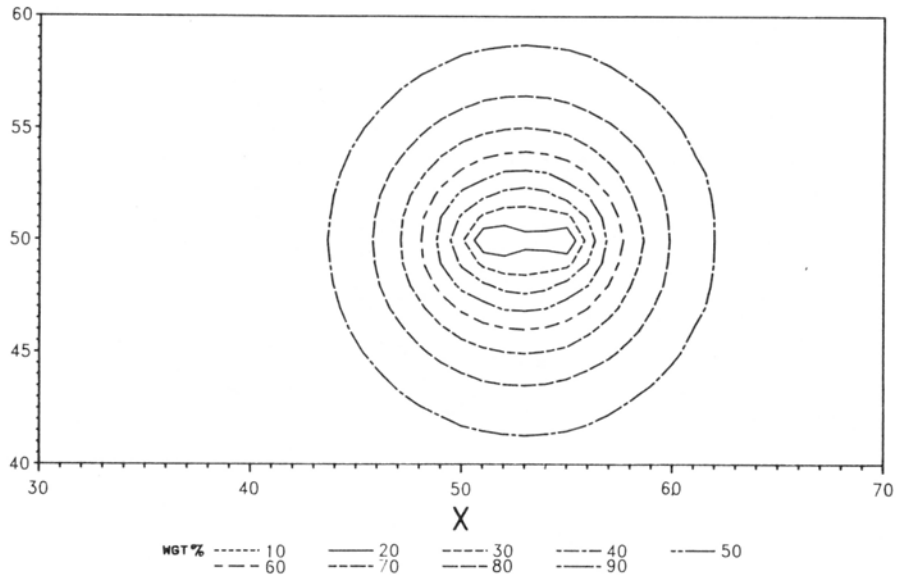

Fig. 8. Relative Weight Function, Detector Angle 30°, for Slab z=2–3

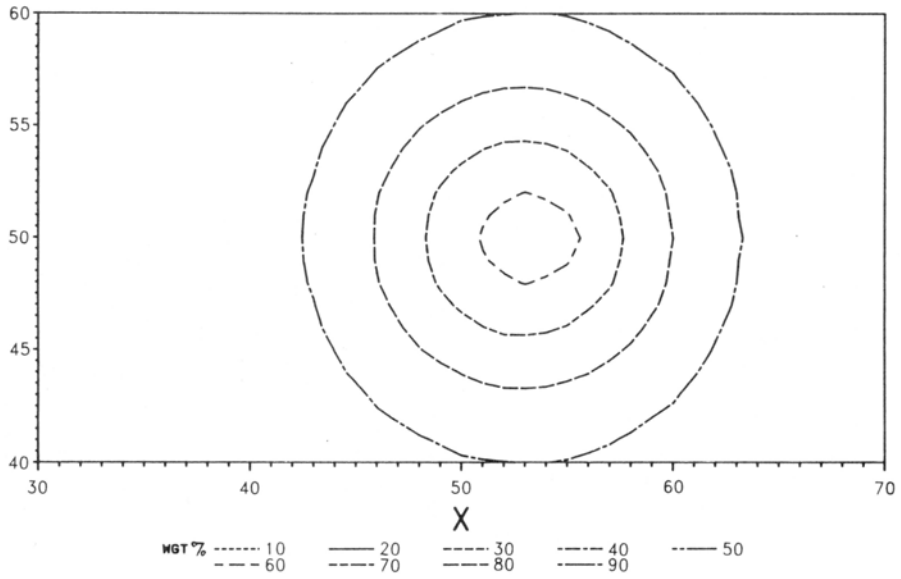

Fig. 9. Relative Weight Function, Detector Angle 30°, for Slab z=6–7

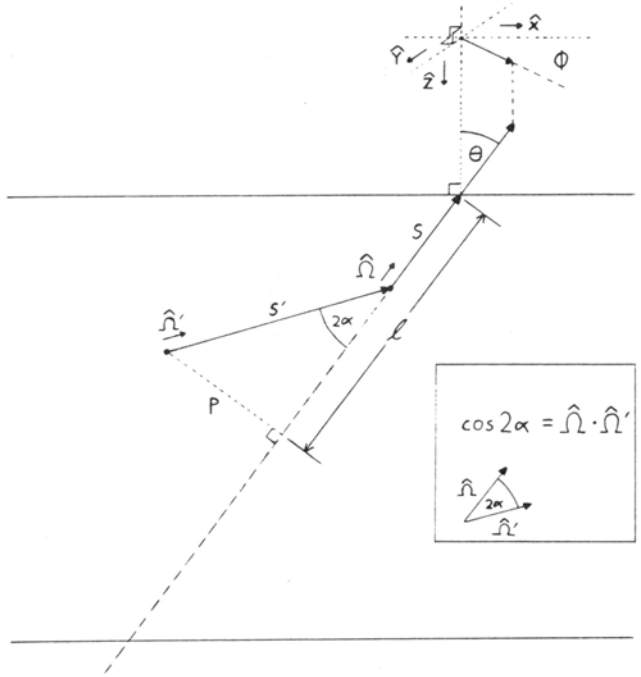

Fig. 10. Geometry for Collimated Detector

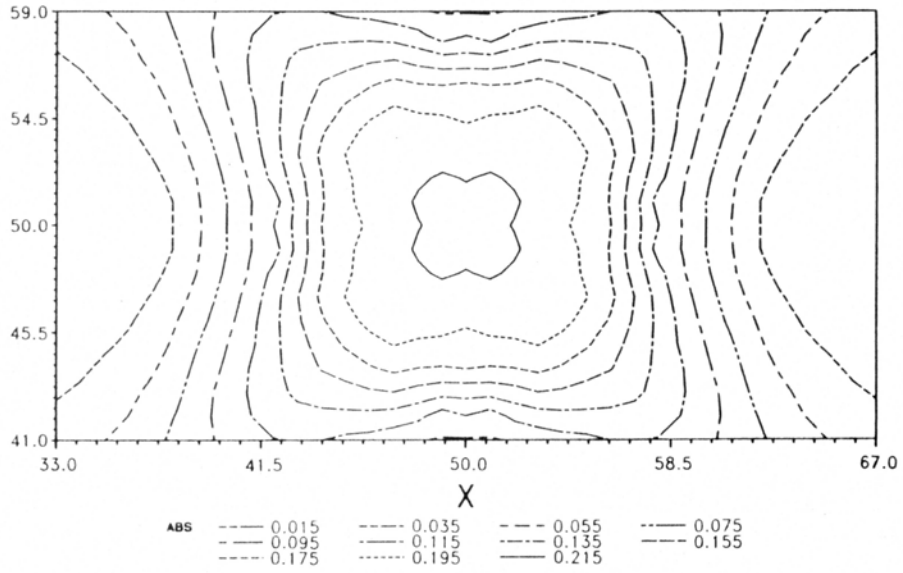

Fig. 11. Image for Sample Absorber Problem, Slab z=4–5

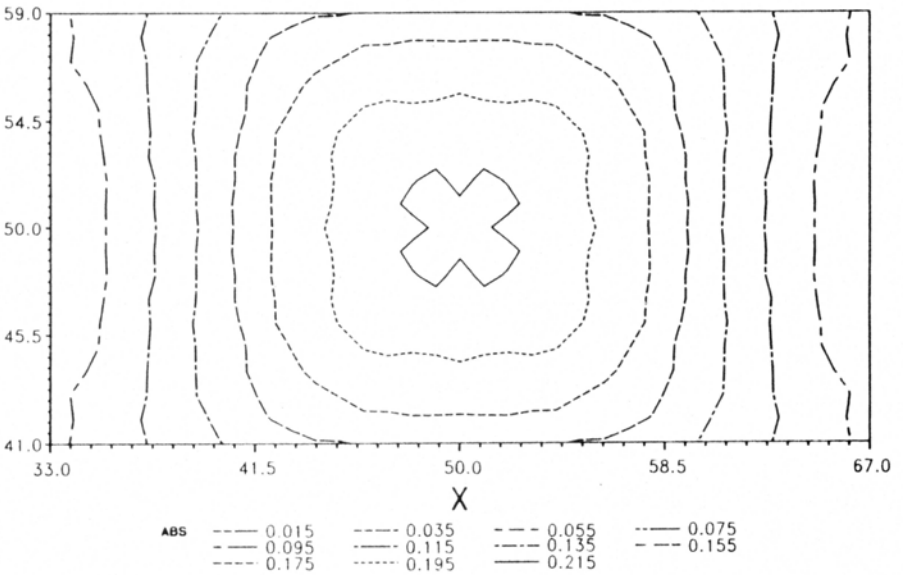

Fig. 12. Image for Sample Absorber Problem, Slab z=11–12